

# Deep Tissue Translocation of Graphene Oxide Sheets in Human Glioblastoma 3D Spheroids and an Orthotopic Xenograft Model

Irene de Lázaro, Paul Sharp, Cansu Gurcan, Ahmet Ceylan, Maria Stylianou, Thomas Kisby, Yingxian Chen, Sandra Vranic, Katharine Barr, Hadiseh Taheri, Asuman Ozen, Cyrill Bussy, Acelya Yilmazer,\* and Kostas Kostarelos\*

Its anatomical localization, a highly heterogeneous and drug-resistant tumor cell population and a “cold” immune microenvironment, all challenge the treatment of glioblastoma. Nanoscale drug delivery systems, including graphene oxide (GO) flakes, may circumvent some of these issues bypassing biological barriers, delivering multiple cargoes to impact several pathways simultaneously, or targeting the immune compartment. Here, the interactions of GO flakes with *in vitro* (U-87 MG three-dimensional spheroids, without stromal or immune compartments) and *in vivo* (U-87 MG orthotopic xenograft) models of glioblastoma are investigated. *In vitro*, GO flakes translocated deeply into the spheroids with little internalization in tumor cells. *In vivo*, intracranially administered GO also show extensive distribution throughout the tumor and demonstrate no impact on tumor growth and progression for the duration of the study. Internalization within tumor cells is also scarce, with the majority of flakes preferentially taken up by microglia/macrophages. The results indicate that GO flakes could offer deep and homogenous distribution throughout glioblastoma tumors and a means to target their myeloid compartment. Further studies are warranted to investigate the mechanisms of GO flakes transport within the tumor mass and their capacity to deliver bioactive cargoes but, ultimately, this information could inform the development of immunotherapies against glioblastoma.

## 1. Introduction

Glioblastoma multiforme, which equates to grade IV glioma, is the most frequent form of cancer of the central nervous system and one of the most aggressive. The current standard of care entails surgical resection followed by radiotherapy, plus concomitant and maintenance chemotherapy with temozolomide.<sup>[1]</sup> However, despite these interventions, the median overall survival (OS) after diagnosis does not surpass the 18-month threshold. Furthermore, antiangiogenic therapy with the anti vascular endothelial growth factor (VEGF) antibody bevacizumab has only shown modest benefit in recurrent glioblastoma and does not significantly extend OS in newly diagnosed patients.<sup>[2]</sup>

Several challenges contribute to the difficulty in treating glioblastoma, which have been extensively reviewed by others.<sup>[3]</sup> First, the anatomical localization of the tumor into one of the body’s most vital organs not only sets hurdles to its complete surgical

Dr. I. de Lázaro, Dr. P. Sharp, M. Stylianou, T. Kisby, Y. Chen, Dr. S. Vranic, Dr. K. Barr, Dr. C. Bussy, Prof. K. Kostarelos  
Nanomedicine Lab, National Graphene Institute and Faculty of Biology, Medicine and Health  
University of Manchester  
AV Hill Building, Manchester M13 9PT, UK  
E-mail: kostas.kostarelos@manchester.ac.uk

Dr. I. de Lázaro  
John A Paulson School of Engineering and Applied Sciences  
Harvard University  
58 Oxford Street Cambridge, MA 02138, USA


Dr. I. de Lázaro  
Wyss Institute for Biologically Inspired Engineering at Harvard University  
3 Blackfan Circle Boston, MA 02115, USA

C. Gurcan, H. Taheri, Dr. A. Yilmazer  
Department of Biomedical Engineering, Faculty of Engineering  
Ankara University  
Ankara 06830, Turkey  
E-mail: ayilmazer@ankara.edu.tr

C. Gurcan, Dr. A. Yilmazer  
Stem Cell Institute  
Ankara University  
Ankara 06520, Turkey

Dr. A. Ceylan, Prof. A. Ozen  
Department of Histology Embryology, Faculty of Veterinary Medicine  
Ankara University  
Ankara 06110, Turkey

Prof. K. Kostarelos  
Catalan Institute of Nanoscience and Nanotechnology (ICN2)  
UAB Campus Bellaterra  
Barcelona 08193, Spain

 The ORCID identification number(s) for the author(s) of this article can be found under <https://doi.org/10.1002/adtp.202000109>

© 2020 The Authors. Published by Wiley-VCH GmbH. This is an open access article under the terms of the Creative Commons Attribution License, which permits use, distribution and reproduction in any medium, provided the original work is properly cited.

DOI: 10.1002/adtp.202000109

resection but is also shielded by the blood–brain barrier (BBB). The BBB complicates access of systemically administered therapeutics to the brain, and the search for strategies that bypass this barrier is a very active field in drug delivery research.<sup>[4]</sup> Additionally, the reported heterogeneity in the molecular signature and mutation load of glioblastoma cells<sup>[5]</sup> brings in a major complication in the search for efficient drugs, as it is unlikely that targeting a single pathway will achieve significant therapeutic outcomes. In fact, no significant progress has been made in the development of new chemotherapies for glioblastoma since the approval of temozolomide in 2005.<sup>[6]</sup> Finally, the immune microenvironment in glioblastoma also appears to be a main culprit of the poor prognosis of the disease. Glioblastomas are “cold” tumors with a paucity of T cells, especially CD8<sup>+</sup> cytotoxic T cells, and a predominant myeloid compartment (about 12% of the tumor mass and 30% of all infiltrating cells) that shows an immunosuppressive M2-like phenotype.<sup>[7]</sup> Glioblastoma cells also contribute to the immunosuppressive microenvironment by secreting and expressing immunosuppressive cytokines and surface proteins, respectively.<sup>[7a]</sup>

The development of nanoscale delivery vectors may offer opportunities to circumvent some of these challenges. For example, nanoparticles can be engineered to efficiently cross the BBB and they can also protect their cargo from degradation in the blood or extracellular space prior to reaching its target.<sup>[8]</sup> A single nanocarrier can also accommodate and deliver various therapeutic agents,<sup>[9]</sup> which is of interest in order to target multiple pathways simultaneously, and the intrinsic properties of some nanomaterials can also be exploited for multimodal therapy. An example is the induction of hyperthermia concomitant with temozolomide delivery.<sup>[10]</sup> In addition, nanoparticles can be decorated with targeting ligands to deliver their cargo to specific cell populations, including glioma cells.<sup>[11]</sup> Overall, nanoscale formulations could improve the treatment of glioblastoma and several clinical trials are underway (see Glaser et al.<sup>[12]</sup>), but only one nanoparticle formulation has so far received regulatory approval for this indication. Nanotherm<sup>®</sup>, a magnetic iron oxide nanoparticle formulation developed to induce hyperthermia, was approved by the European medicines agency (EMA) in 2011.<sup>[13]</sup>

Graphene oxide (GO), a relatively recent addition to the nanomaterial toolbox, offers several advantages over other nanocarriers. First, its two-dimensional (2D) structure in the form of oxidized graphene sheets provides a large surface-to-volume ratio that offers increased loading capacity compared to other nanoparticles. The presence of multiple oxygen functionalities grants high dispersibility in aqueous-based biological fluids and also allows covalent and noncovalent conjugation possibilities with chemically diverse small molecules and biologicals.<sup>[14]</sup> GO is also internalized by phagocytic and nonphagocytic cells with very low cytotoxicity.<sup>[14c,15]</sup> Overall, GO represents the most widely studied 2D material as a delivery vector in vitro and in preclinical models in vivo,<sup>[14b,14c,15,16]</sup> even though its interactions with relevant models of glioblastoma remain poorly described.<sup>[17]</sup> Here, we aimed to take a first step toward the investigation of GO as a potential delivery vector for the treatment of glioblastoma. We characterized the interactions of thin, biomedical-grade GO flakes (i.e., endotoxin-free and highly dispersible in biological fluids) of controlled dimensions (lateral size < 1 μm, thickness 1–2 nm) with in vitro (3D spheroids) and

in vivo (orthotopic xenograft) models of the disease. We report extensive translocation of the material throughout the tumor mass and preferential internalization by the macrophage compartment in vivo, which may offer an opportunity to utilize GO as delivery vector targeting this cell population in glioblastoma.

## 2. Results

Throughout this work, we used endotoxin-free GO flakes of average lateral dimensions of a few hundred nm prepared by a modified Hummers' method.<sup>[18]</sup> A summary of the physicochemical characterization of the GO flakes utilized in our study, which have been described in a previous publication,<sup>[19]</sup> is provided in Table S1 in the Supporting Information. These GO sheet suspensions have been shown to be noncytotoxic in a number of cell lines at the range of concentrations studied here.<sup>[15,20]</sup> We additionally confirmed the absence of cytotoxicity induced by the material in Uppsala 87 Malignant Glioma (U-87 MG) cells specifically (Figure S1, Supporting Information).

### 2.1. GO Induces U-87 MG Spheroid Growth without Cell Proliferation

To investigate the interactions of GO with glioblastoma cells, we first exposed 3D spheroids composed of human U-87 MG glioma cells to 10 or 100 μg mL<sup>-1</sup> of GO flakes, dispersed in the cell culture medium, and measured spheroid growth for 12 d. We used spheroids because they recapitulate the 3D in vivo architecture of the tumor and its cell–cell interactions more closely than 2D monolayers.<sup>[21]</sup> Spheroids were prepared from U-87 MG single cell suspensions and left to form for 3 d prior to GO exposure. GO induced a dose-dependent increase in spheroid diameter (Figure 1a). From day 2 after exposure, statistically significant differences in spheroid size were observed, and those became larger over time (Figure 1b, *p*-values are shown in Table S2, Supporting Information). We used light sheet fluorescence microscopy (LSFM) 7 d after treatment to confirm that the exposure to GO induced an increase in tumor spheroid volume (X/Y/Z directions) and not just in a 2D plane (data not shown). However, several observations suggested that the increase in size was not a result of cell division. First, we enzymatically dissociated individual U-87 MG spheroids into single-cell suspensions, 10 d after GO exposure, and counted the number of cells with a hemocytometer. No significant differences were found in the cell number per spheroid among treatment groups (Figure 1c). Next, we sought to obtain more precise information on potential differences in the rate of cell division, as errors could be introduced due to cell loss or incomplete dissociation when generating a single-cell suspension. We performed immunohistochemistry (IHC) to detect Ki67, a marker of cell proliferation, in cryosections obtained from U-87 MG spheroids 7 d after exposure (Figure 1d) and quantified the abundance of Ki67<sup>+</sup> cells (Figure 1e). A small but significant decrease in the number of proliferating Ki67<sup>+</sup> cells was observed in GO-treated spheroids, which was also dose dependent (Figure 1e). This observation was also supported by the levels of Ki67 mRNA measured by real-time quantitative reverse transcription polymerase chain reaction (RT-qPCR), which were significantly

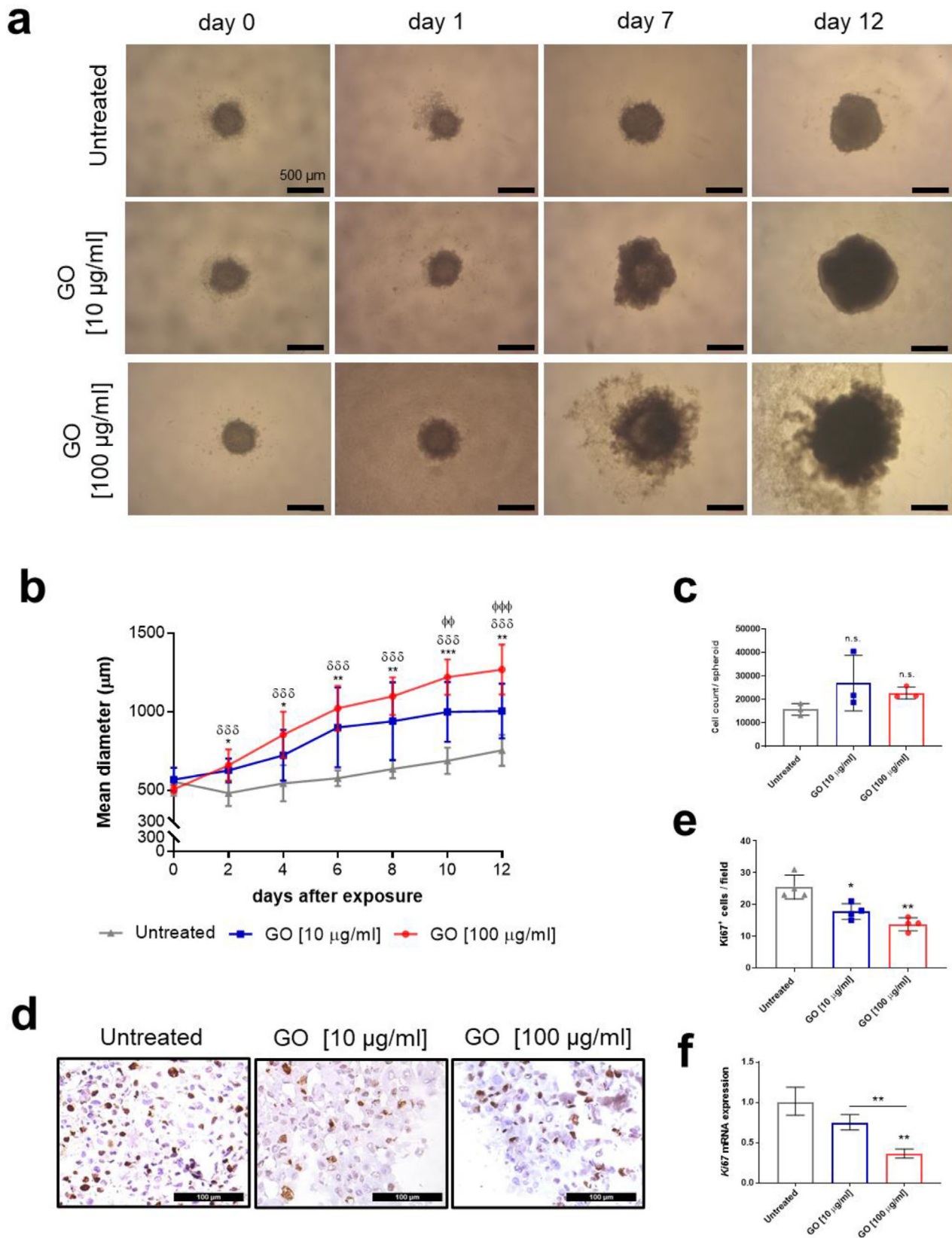


**Figure 1.** Exposure to GO induces U-87 MG spheroid volume growth, in a dose-dependent manner, without cell proliferation. U-87 MG spheroids were exposed to 0, 10, and 100 µg mL<sup>-1</sup> GO in the cell culture medium. a) Images of spheroids 0, 1, 7, and 12 d after exposure (scale bars represent 500 µm).

downregulated with the GO treatment 12 d after exposure (Figure 1f). Overall, these results confirmed that the exposure of U-87 MG spheroids to GO flakes in vitro correlated with a significant increase in spheroid volume but a decrease in tumor cell proliferation.

## 2.2. GO Flakes Translocate Deeply into U-87 MG Spheroids but Remain Primarily within the Extracellular Compartment

We next set out to investigate the distribution of GO flakes within the spheroid 3D structure. The optical properties of GO allow label-free detection of the material by fluorescence microscopy.<sup>[20]</sup> LSFM of whole mount spheroids exposed to GO for 24 h showed penetration of the material for several layers of cells. Figure 2 shows optical sections taken at different depths from the front to the back of the spheroid. Next, ultrathin sections of U-87 MG spheroids were obtained 7 d after GO exposure, for further investigation. Toluidine B staining analyzed by brightfield microscopy demonstrated the increased accumulation of extracellular matrix (ECM) in GO-treated spheroids, in a dose-dependent fashion (gray, unstained areas, compared to purple-stained ones, Figure 3a), which quite likely accounted for the increase in spheroid volume reported in our study. These data further supported our previous observation that the GO-induced increase in spheroid volume was not linked to an increase in cell proliferation.

We next performed Raman mapping of neighboring spheroid sections to localize the distribution of GO flakes (Figure 3b). This technique, and the use of sections, allowed us to investigate the presence of GO at the core of the spheroids with more confidence. No Raman fingerprints specific to GO were found in the control nontreated spheroids. In contrast, when spheroids were exposed to either 10 or 100  $\mu\text{g mL}^{-1}$  of GO flakes, clear Raman spectra specific to GO fingerprints, including D and G bands at about 1352 and 1594  $\text{cm}^{-1}$ , respectively, could be identified within the sections (shown in green in the maps, Figure 3b). More interestingly, when increasing the concentration from 10 to 100  $\mu\text{g mL}^{-1}$ , the mapping revealed that a larger surface of the spheroids was positive for GO fingerprints, which confirms again that the accumulation of GO flakes in spheroids is a dose-dependent phenomenon. In addition, GO positive regions were identified not only at the rim but also at the core of the spheroid. This supported our LSFM observations that GO translocated deeply into the spheroids. Poor penetration into 3D tissues is indeed a limitation suffered by a plethora of nanoparticles that perform well when tested in 2D monolayers, but fail to translocate sufficiently and evenly into 3D structures resembling solid tumors.<sup>[21a]</sup> Figure S2 in the Supporting Information

shows brightfield images of tissue sections utilized for Raman mapping, as well as the individual maps of different regions of each spheroid that have been combined in Figure 3b. Further details of Raman data acquisition and analysis are provided in Figure S2 and Table S3 in the Supporting Information.

We also performed transmission electron microscopy (TEM) in nearby sections, which provided much higher resolution than LSFM or Raman mapping, to confirm the subcellular localization of GO flakes (Figure 3c). The material accumulated predominantly in the extracellular space, with minimal intracellular localization, although we were able to identify various cells in which a small amount of GO was internalized in vacuole-like structures (blue arrows). We also observed a small number of cells preparing to uptake the material (green arrows). To further interrogate the scarce cellular uptake of GO sheets in the spheroids, we exposed U-87 MG cells grown in 2D monolayers to the same concentrations of the material (Figure S3, Supporting Information). The fluorescence signal of GO was barely observed in the intracellular space by confocal microscopy throughout the culture, as opposed to previous studies using different cell types exposed to the same concentrations of the same material.<sup>[15,20]</sup> This further confirmed the very limited degree of cellular uptake and internalization obtained within the 3D spheroids.

Transport of GO from the periphery to the core of the spheroids could be ascribed to either a dynamic process mediated by cell-to-cell transfer (i.e., transcytosis-like)<sup>[22]</sup> or a passive mechanism via diffusion in the extra-cellular space, in between adjacent cells. Considering the scarce evidence of cellular internalization found here, the latter is the most plausible mechanism. In addition, TEM images also evidenced an increase in the abundance of collagen-like fibers within the extracellular space of GO-treated spheroids (indicated with red arrows in Figure 3c). This aligned well with our observation of an increased presence of ECM upon GO treatment using toluidine blue staining. Overall, these results confirmed that GO is barely internalized by U-87 MG cells. Instead, it translocated deeply into 3D spheroids, most likely through the extracellular space, and could be responsible for triggering the increased secretion of ECM components by the cells within the spheroids.

## 2.3. GO Has Minimal Impact on the Transcriptomic and Proteomic Signatures of U-87 MG Spheroids

We then examined whether the exposure to GO induced changes in gene and protein expression in U-87 MG cells. Previous studies using other cell lines have demonstrated that GO can have significant impact in gene expression, even in transcripts that are usually utilized as reference or housekeeping genes.<sup>[16b,23]</sup> For

b) Spheroid growth curve. Data show mean diameter  $\pm$  SD,  $n = 12$ . \* $p < 0.05$ , \*\* $p < 0.01$ , and  $p < 0.001$  indicate statistically significant differences between untreated and  $[\text{GO}] = 10 \mu\text{g mL}^{-1}$  groups.  $\delta\delta\delta p < 0.001$  indicates statistically significant differences between untreated and  $[\text{GO}] = 100 \mu\text{g mL}^{-1}$  groups.  $\phi\phi\phi p < 0.01$  and  $\phi\phi\phi\phi p < 0.001$  indicate statistically significant differences between  $[\text{GO}] = 10 \mu\text{g mL}^{-1}$  and  $[\text{GO}] = 100 \mu\text{g mL}^{-1}$  groups. Statistics were assessed by one-way ANOVA and Tukey's post hoc test or by Welch ANOVA and Games-Howell post hoc test, depending on the homogeneity of variance, and a summary is presented in Table S2 in the Supporting Information. c) Cell counting upon spheroid dissociation (10 d after treatment) shows no statistically significant (n.s.) differences in the number of cells among treatment groups, assessed by one-way ANOVA and Tukey's post hoc test,  $n = 3$ . Data are presented as mean  $\pm$  SD. d) Ki67 was detected in spheroid sections fixed 7 d after treatment by IHC and e) Ki67<sup>+</sup> cells were quantified in four random fields per condition; \* $p < 0.05$  and \*\* $p < 0.01$  indicate statistically significant differences, assessed by one-way ANOVA and Tukey's post hoc test ( $n = 4$ ). Data are shown as mean  $\pm$  SD. f) Ki67 mRNA levels were assessed by real-time RT-qPCR on day 12 after exposure. \* $p < 0.05$  and \*\* $p < 0.01$  indicate statistically significant differences, assessed by one-way ANOVA and Tukey's post hoc test, ( $n = 3$ ). Data are shown as mean fold change  $\pm$  propagated error.

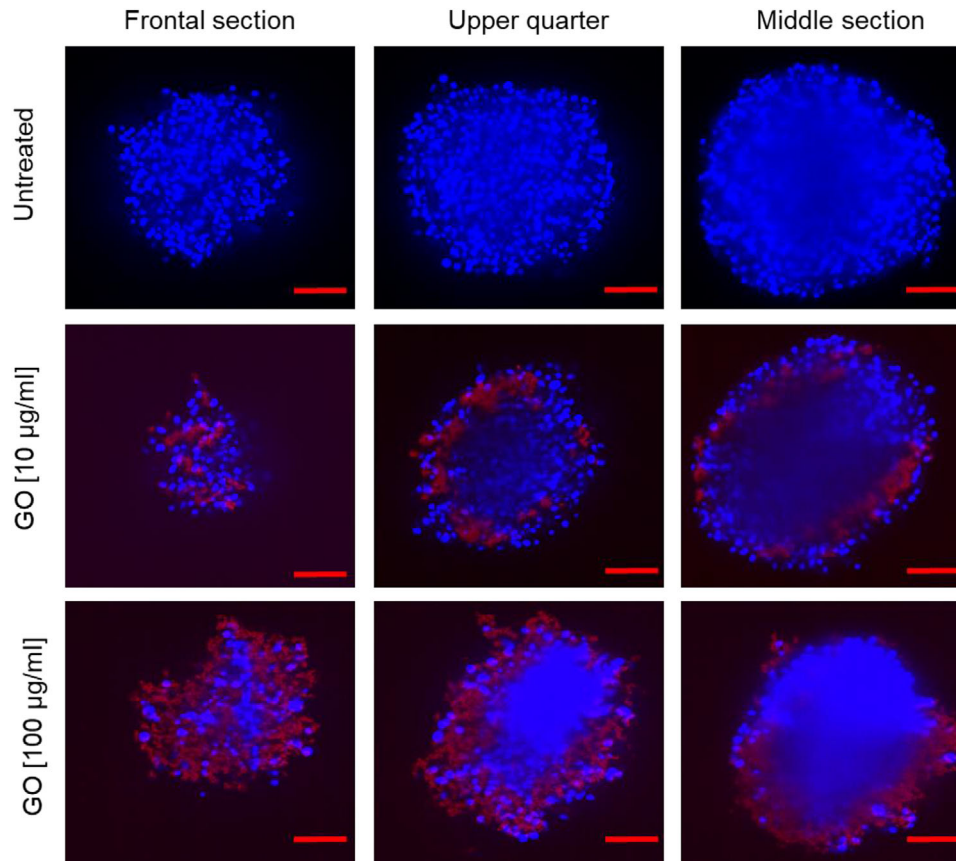


**Figure 2.** GO penetrates in U-87 MG spheroids but remains in the extracellular space. Images of spheroids one day after exposure to 0, 10, and 100  $\mu\text{g mL}^{-1}$  GO, acquired using Lightsheet Z.1 fluorescence microscope. Frontal, upper quarter, and middle sections of the spheroids are shown. DAPI staining is shown in blue and GO autofluorescence signal is shown in magenta. Scale bars indicate 100  $\mu\text{m}$ .

this reason, we first determined the stability of the expression of ten different candidate reference genes upon exposure of U-87 MG spheroids to different doses of GO, and selected the combination of *GAPDH* and *MAPK1* as the most stable normalization factor for further gene expression studies, according to the Normfinder algorithm (Figure S4, Supporting Information). We then performed real-time RT-qPCR to investigate the mRNA levels of several genes involved in critical pathways in glioblastoma (Figure S5, Supporting Information). A total of 87 transcripts involved in proliferation (Figure S5a, Supporting Information), apoptosis (Figure S5b, Supporting Information), invasion and migration (Figure S5c, Supporting Information), integrins involved in cell migration (Figure S5d, Supporting Information), proteases involved in ECM remodeling (Figure S5e, Supporting Information), genes involved in ECM deposition (Figure S5f, Supporting Information), angiogenesis and hypoxia (Figure S5g, Supporting Information), and other markers of glioblastoma (Figure S5h, Supporting Information) were investigated. Table S4 in the Supporting Information includes information related to all such genes and the primer pairs utilized in this study. *P*-values for genes that showed statistically significant changes in mRNA expression are given in Table S5 in the Supporting Information (10  $\mu\text{g mL}^{-1}$  dose) and Table S6 in the Supporting Information (100  $\mu\text{g mL}^{-1}$ ). Changes in gene expression were very small. At the lowest GO dose (10  $\mu\text{g mL}^{-1}$ ), only

*TIMP2* (fold change = 1.55) and *LAMB1* (1.34) were upregulated 24 h after exposure (Table S5, Supporting Information). On day 7, we only confirmed the upregulation of *MMP9* (1.68) and *IDH1* (1.34) and the downregulation of *NES* (0.54). 12 d after exposure, only *LAMB1* was slightly downregulated (fold change = 0.80) compared to untreated controls. The highest dose of GO (100  $\mu\text{g mL}^{-1}$ ) induced changes in a slightly larger number of transcripts, but fold changes were also small (all fold changes < 2.6, Table S6, Supporting Information). Most differentially expressed genes were involved in ECM deposition or remodeling and cell–cell adhesions. However, we did not find a clear pattern among the transcripts under study, since some of them were down- and others upregulated after GO treatment (Figure S5 and Tables S5 and S6, Supporting Information).

Prompted by the very few changes observed in the genes interrogated, which we selected based on their relevance to glioblastoma progression, we decided to perform a broader, unbiased analysis of changes at the protein expression level (Figure 4). For that, we performed liquid Chromatography with tandem mass spectrometry (LC-MS/MS) upon exposure of U-87 MG spheroids to the highest dose of GO (100  $\mu\text{g mL}^{-1}$ ). Principal component analysis (PCA) demonstrated that the samples clustered according to experimental conditions, namely GO treatment or no treatment (Figure 4a). Investigation of differentially expressed proteins confirmed that only 37 out

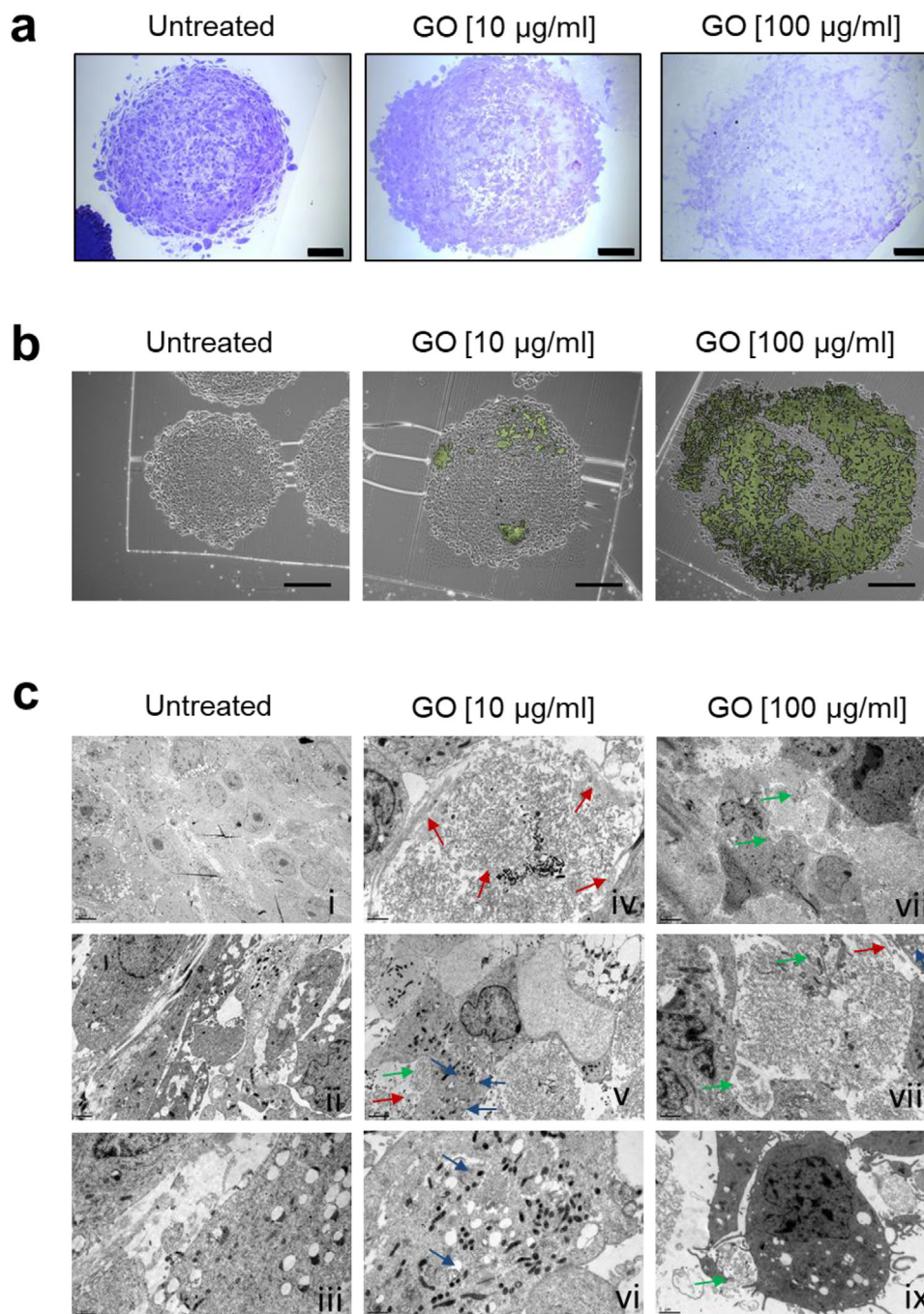


**Figure 3.** GO distributes primarily within the extracellular space of U-87 MG spheroids and correlates with increased deposition of ECM. Spheroid sections were fixed 7 d after exposure to 0, 10, or 100  $\mu\text{g mL}^{-1}$  GO. a) Toluidine blue staining of U-87 MG spheroid sections shows increased accumulation of ECM (gray areas) with increasing doses of GO. Scale bars indicate 100  $\mu\text{m}$ . b) Chemical mapping by Raman spectroscopy imaging confirms dose-dependent distribution of GO flakes which is not limited to the rim of the spheroid but reaches the core, scale bars indicate 100  $\mu\text{m}$ . c) GO flakes are clearly visible in the extracellular space of U-87 MG spheroids in TEM images, but intracellularly located GO is scarce. Red arrows indicate collagen fibers. Green arrows indicate cells preparing to phagocytize GO flakes. Blue arrows indicate vacuoles containing GO. Scale bars represent 1 or 5  $\mu\text{m}$  as indicated in the images.

of 1698 proteins were differentially expressed compared to untreated controls (Figure 4b and Tables S7 and S8, Supporting Information). These results further supported our observation that the changes in the molecular signatures of U-87 MG cells upon exposure to GO were very small. Gene ontology analysis of

differentially expressed proteins retrieved terms related to endocytosis, phagocytosis, and vesicle transport as the most enriched biological process terms (Figure 4c). Cellular compartment gene ontology terms also included terms related to endocytic and cytoplasmic vesicles, as well as collagen containing-extracellular

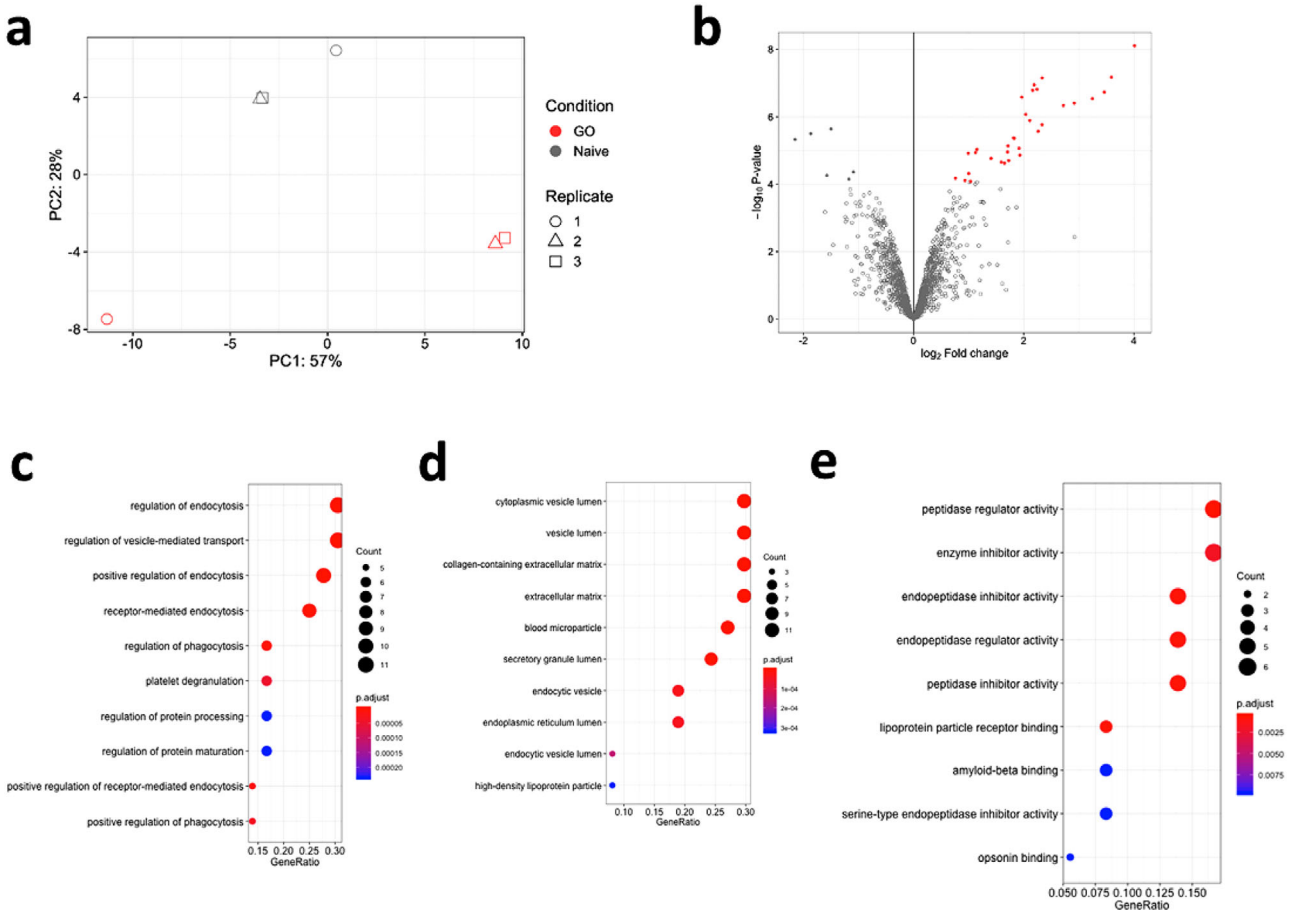


**Figure 4.** Exposure to GO flakes induces minor changes in U-87 MG protein expression. U-87 MG spheroids treated for 7 d with the highest dose of GO ( $100 \mu\text{g mL}^{-1}$ ), or left untreated, were processed for proteomics analysis ( $n = 3$ ). a) PCA with all detected proteins indicated that the samples clustered according to treatment. b) Volcano plot shows differentially expressed proteins between the groups, obtained with the DEP package of Bioconductor. Fold changes were calculated normalizing to the untreated group. The Clusterprofiler package (Bioconductor) was implemented to perform Gene Ontology. Dot plots show c) biological process, d) cellular compartment, and e) molecular function Gene Ontology terms.

matrix and extracellular matrix, that scored as the 3rd and 4th most enriched terms, respectively (Figure 4d). Finally, molecular function terms included several related to peptidase activity (Figure 4e).

Overall, these analyses demonstrated that the exposure of U-87 MG spheroids to GO only induced minor changes in the expression of a small number of genes and proteins, most of them likely related to the attempts of the cells to uptake the material and to the increased generation of ECM. This contrasts with the observations found in other cell types, in which changes in gene and protein expression were much more remarkable.<sup>[16b,23]</sup> However, this could be linked to the much lower internalization of the material in U-87 MG cells.

#### 2.4. Stereotactic, Intratumorally Administered GO Sheets Distribute Extensively throughout the Tumor Volume and Are Internalized by Resident Microglia/Macrophages in vivo

While 3D in vitro tumor models better represent the in vivo scenario than their 2D counterparts, they are still far from fully

recapitulating the in vivo microenvironment. In particular, the model utilized here did not account for the presence of the stromal, vascular, and immune compartments in glioblastoma, among other factors. For this reason, we set out to determine the fate and effects of GO sheets following direct intratumoral injection in an orthotopic xenograft model of glioblastoma. U-87 MG cells were implanted intracranially in athymic nude mice and tumors were left to grow for 16 d after inoculation. At this point, mice received a second intracranial administration of either 1  $\mu\text{L}$  of dextrose (vehicle control), 0.1  $\text{mg mL}^{-1}$  GO, or 1  $\text{mg mL}^{-1}$  GO. Magnetic resonance imaging (MRI) of the tumor volume over time demonstrated no significant differences in the evolution of tumor growth across treatment groups, for the duration of the study, contrary to our observations in vitro (Figure 5a,b). In addition, no differences were observed in the survival of the mice for the duration of the study. Tumor volume was also measured from the reconstruction of H&E stained brain tissue sections, which confirmed the absence of differences in tumor size between groups (Figure 5c). These results suggested that intratumoral administration of GO did not significantly impact glioblastoma progression in the timeframe

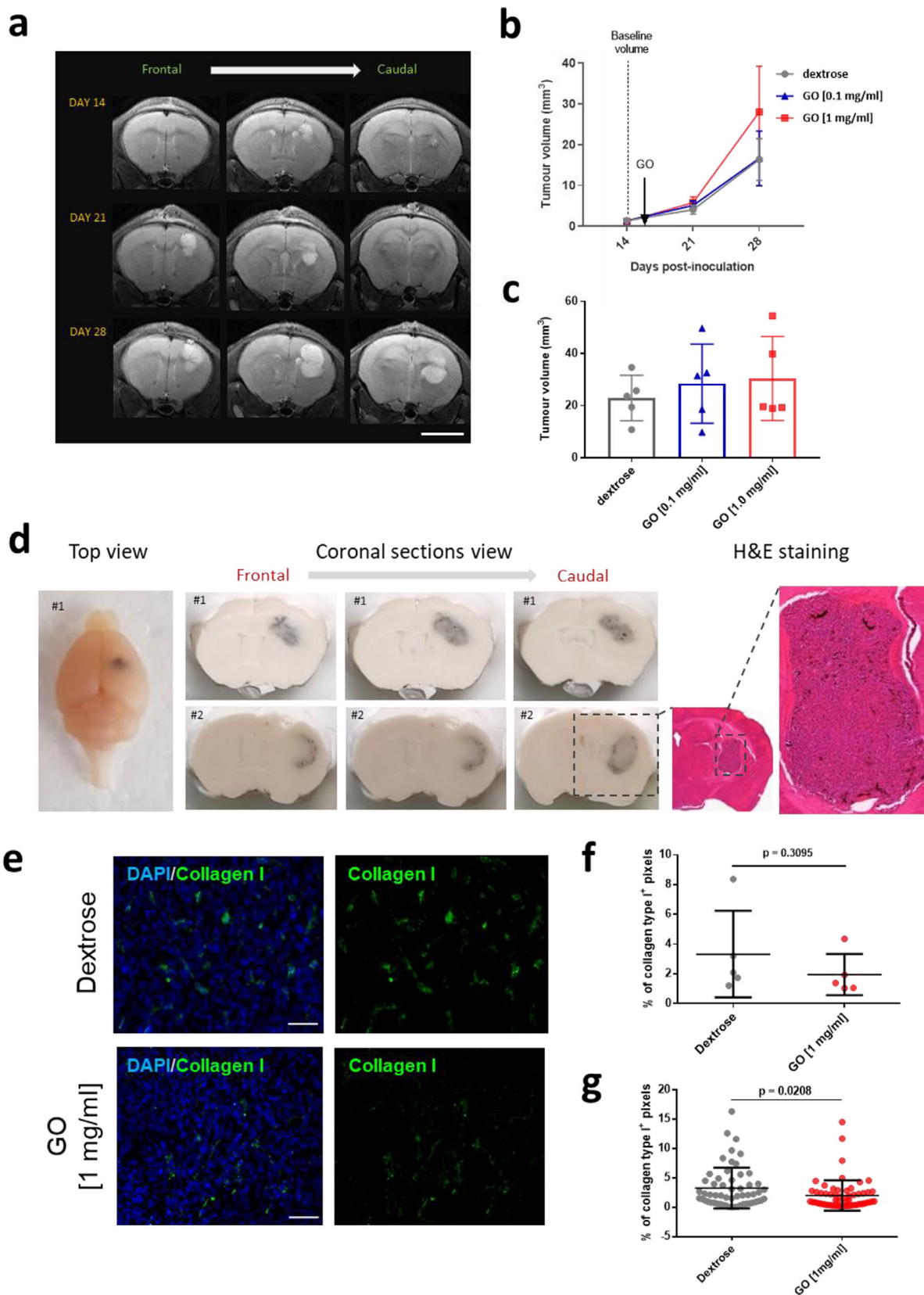


**Figure 5.** GO administered intratumorally distributes extensively in a U-87 MG orthotopic xenograft and does not induce tumor growth or ECM deposition. Athymic nude mice were implanted with  $1 \times 10^5$  U-87 MG cells, in  $1 \mu\text{L}$  PBS, into the right striatum and intracranially administered with  $1 \mu\text{L}$  of 5%



of our study (28 d after tumor cell inoculation). In addition, histological investigation of the brains 12 d after intratumoral delivery of GO showed that the material had distributed extensively throughout the entire volume of the tumor but remained largely confined to its margins (Figure 5d). The extraordinary distribution of GO throughout the tumor, in spite of the small volume that was administered (1  $\mu\text{L}$ ), has important implications in the potential of GO as a delivery vector for glioblastoma therapies.

Since we did not observe any significant increases in tumor volume in vivo following GO treatment, contrary to our observations in spheroids in vitro, we decided to investigate the deposition of ECM in the tissue. We did not observe differences in the deposition of collagen I in the tumor when GO was administered (Figure 5e–g). The lack of increased ECM deposition is in marked contrast to the results of in vitro spheroids, so we next examined the subcellular distribution of the material in vivo (Figure 6). We stained brain tumor sections from U-87 MG glioma mice administered with GO for IBA1<sup>+</sup> cells, which are primarily macrophages and microglia. We used phase contrast light microscopy to identify GO (black particles) and fluorescence microscopy to detect IBA1<sup>+</sup> cells (Figure 6a). The data showed that >60% of GO particles identified were internalized by IBA1<sup>+</sup> cells (Figure 6b). Because some glioma cells, including U-87 MG, can upregulate IBA1,<sup>[24]</sup> we also costained brain tissue sections with an antibody against human mitochondria (Mit) that allowed us to identify whether IBA1<sup>+</sup> cells have mouse (macrophages/microglia) or otherwise human (U-87 MG) origin (Figure 6c). Approximately 20% of GO particles colocalized with IBA1<sup>+</sup>/Mit<sup>+</sup> double positive cells (i.e., originated from the U-87 MG xenograft, Figure 6d). This result was expected since we observed some, albeit low, internalization of GO flakes in glioblastoma cells in vitro. Overall, these results demonstrated that intratumoral administration of GO results in a predominant internalization of the nanomaterial by macrophages and microglia infiltrating the tumor, and that GO penetrates readily throughout the tumor with no significant impact on tumor growth or progression. Given the crucial role that macrophages and microglia play in the establishment of the immunosuppressive microenvironment in glioblastoma,<sup>[7b]</sup> these observations warrant the further investigation of GO as a vector system in the context of glioblastoma immunomodulation.

### 3. Discussion

This study described the interactions of GO flakes with two models of glioblastoma (in vitro and in vivo) as an initial step toward investigation of this material as a delivery platform technology for the treatment of glioblastoma. In vitro studies with 3D U-87 MG spheroids helped us determine the interactions and effects of GO in glioblastoma tumor cells alone (in the absence of an immune component). We have demonstrated that GO sheets transported and localized at the extracellular space throughout the spheroid volume, and that the material was scarcely internalized by this tumor cell type (Figure 3c and Figure S4, Supporting Information) with no cytotoxicity at the dose-range studied (Figure S1, Supporting Information). Our cell internalization results are in agreement with another previous report indicating strong interactions of GO flakes with the plasma membrane, but very poor uptake in U-87 MG and other glioma-like cells (at least three times lower than other carbon nanomaterials).<sup>[17a]</sup> The lack of cytotoxicity of GO in glioma cells has also been reported by others, who also demonstrated its lack of genotoxicity.<sup>[17b]</sup> More studies are warranted in order to reveal the mechanisms of GO sheet interaction with glioblastoma and other cancer cell types both in monolayer and 3D conformation.

We did observe an increase in the deposition of ECM upon exposure of U-87 MG spheroids to GO in vitro (Figure 3a,c and Figure S2, Supporting Information). Indeed, many of the few changes observed at the gene and protein levels were related to ECM deposition and remodeling, according to gene ontology (Figure 4). Because such processes are frequently utilized by cancer cells, including glioma cells, to migrate and infiltrate the tissues,<sup>[25]</sup> this could potentially be a source of concern on the safety of the material in its interaction with glioblastoma. However, we confirmed that there were no alterations in ECM deposition when the material was administered in vivo (Figure 5d). This discrepancy could be due to the predominant sequestration of GO sheets by macrophages and microglia in the orthotopic model (Figure 6). The increased deposition of ECM in GO treated spheroids is likely responsible for their dose-dependent increased volume, which we confirmed was not caused by higher levels of tumor cell proliferation. Again, these changes in tumor size were only observed in vitro and, overall, these findings highlight the inadequacy of oversimplified in vitro models (even if in 3D) to recapitulate the in vivo scenario and

dextrose, 0.1 mg mL<sup>-1</sup> of GO, or 1 mg mL<sup>-1</sup> GO 17–21 d later ( $n = 5$ ). For longitudinal assessment of tumor growth, tumor bearing mice underwent MRI ( $n = 2$  for dextrose,  $n = 3$  for GO groups). a) Representative  $T_2$ -weighted gradient echo MRI images for a vehicle (5% dextrose) control mouse showing intracranial tumor growth. Baseline tumor volumes were measured 14 d post tumor inoculation (p.i.) to demarcate the center of the tumor for subsequent intratumoral administration of dextrose or GO. MRI was repeated on days 21 and 28 d p.i., to determine the effect of GO on tumor growth. Scale bar, 4 mm. b) MRI longitudinal assessment of tumor volume in dextrose and GO groups. Data are displayed as mean tumor volume  $\pm$  standard error (SE). No statistical significance was found between the groups, assessed by one-way ANOVA. c) Tumor volume calculated from H&E stained sections 28 d p.i. from dextrose ( $n = 5$ ) and GO treated mice (1.0 or 0.1 mg mL<sup>-1</sup>,  $n = 5$  for each group). Data are displayed as mean tumor volume  $\pm$  SD and each dot represents an individual tumor. No statistical significance was found between GO treated mice and vehicle controls (one-way ANOVA). d) GO distribution in intracranial tumors from two mice, 12 d after direct intratumoral injection of 1 mg mL<sup>-1</sup> GO (1  $\mu\text{L}$ ). The images of frozen brains undergoing cryosectioning clearly show diffusion of the material throughout the tumor. H&E staining of the tissue indicates that GO remains confined within the tumor boundaries. e) Collagen I (green) and DAPI (blue) staining performed in brain sections collected 12 d after GO administration. Scale bar, 20  $\mu\text{m}$ . f) Quantification of collagen I staining per field of view. Each dot represents the average number of collagen I positive pixels in three randomly selected fields of view within the brain tumor area, four tissue sections per animal,  $n = 5$  animals per group.  $P$ -values indicated on the graph were assessed using a Mann–Whitney  $U$  test. g) Quantification of collagen I staining per field of view. Each dot represents the number of collagen I positive pixels in a randomly selected field of view within the brain tumor area. Three random fields of view per section, four tissue sections per animal,  $n = 5$  animals per group.  $P$ -values indicated on the graph were assessed using a Mann–Whitney  $U$  test.

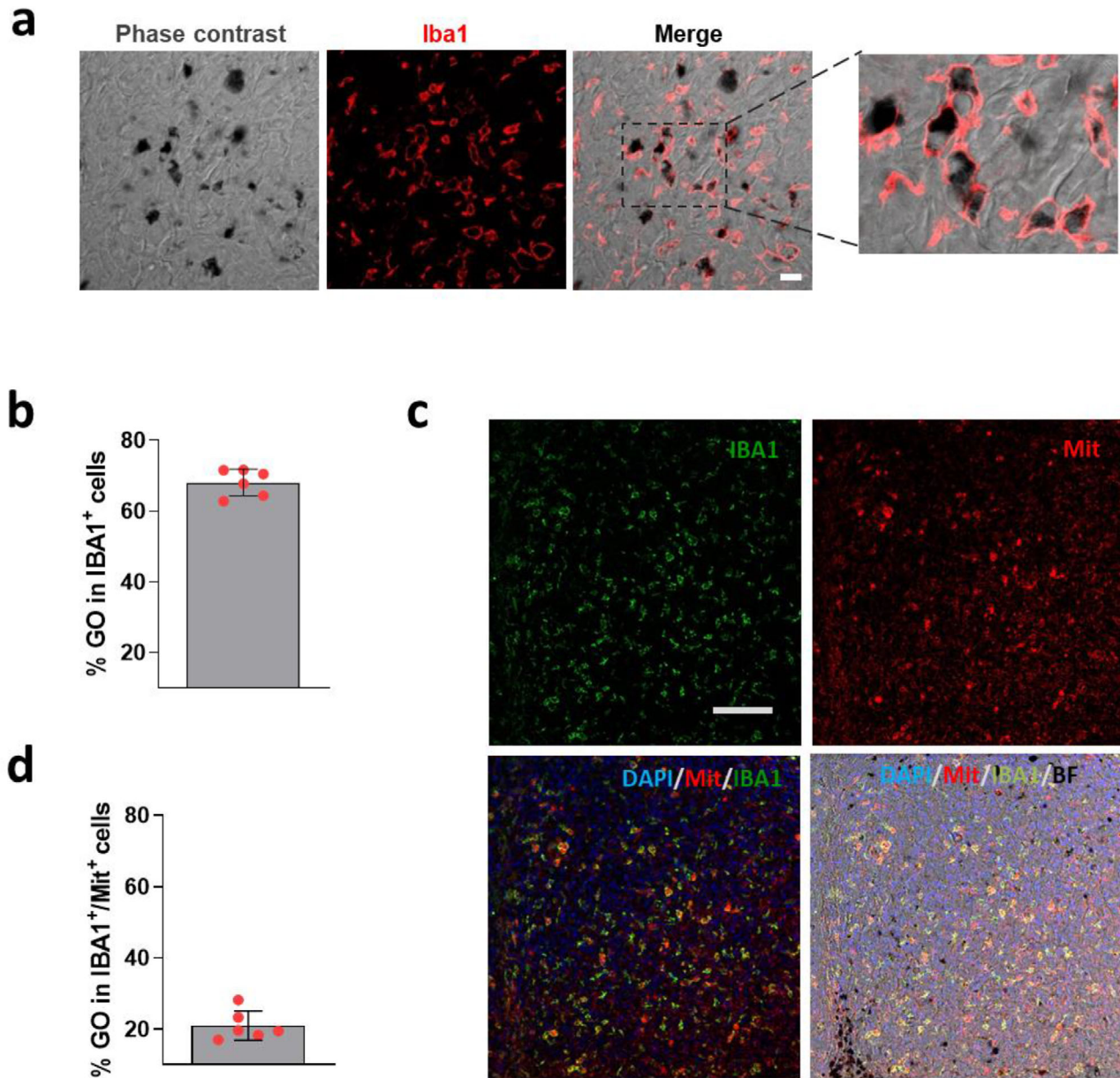


**Figure 6.** Intratumorally injected GO is predominantly internalized by IBA1<sup>+</sup> macrophages and microglia. a) Representative bright-field (phase-contrast) and immunofluorescence images of U-87 MG xenografts collected 12 d after dextrose or 1 mg mL<sup>-1</sup> GO administration ( $n = 5$ ) show predominant localization of GO (black) in IBA1<sup>+</sup> cells (red). Scale bar, 20  $\mu$ m. b) Quantification of the percentage of GO (black particles) in IBA1<sup>+</sup> cells. Each dot represents the average of quantified GO particles in two fields of view from three separate frozen brain tumor sections per animal,  $n = 6$  per group. c) Representative bright-field (phase-contrast) and immunofluorescence images of IBA1 and human mitochondria (Mit) staining. d) Quantification of the percentage of GO (black particles) in IBA1<sup>+</sup>/Mit<sup>+</sup> cells (human origin). Each dot represents the average of quantified GO particles in two fields of view from three separate frozen brain tumor sections per animal,  $n = 5$  per group.

confirm that the results obtained in such systems should be interpreted with caution. Indeed, there is an urgent need for more physiologically relevant ex vivo models that not only recapitulate the 3D architecture of the tissue, but also integrate stromal and immune compartments, perfusable vasculature and that mimic the chemical and mechanical properties of the in vivo ECM.<sup>[26]</sup>

One of the most interesting findings from this study was the preferential uptake of intratumorally administered GO

flakes by IBA1<sup>+</sup> macrophages and microglia in the orthotopic xenograft model (Figure 6). These cell types acquire a M2-like phenotype within the tumor which is partially responsible for the immunosuppressive microenvironment that contributes to the poor prognosis of glioblastoma.<sup>[7b]</sup> Due to its detrimental role in this and other so-called “cold tumors”, there is an increasing number of strategies aiming to either deplete or reprogram the macrophage compartment toward a M1-like “tumoricidal”

or “proinflammatory” phenotype.<sup>[27]</sup> Different approaches have explored a plethora of pathways including macrophage depletion with small molecule inhibitors or antibodies against the colony-stimulating factor 1 (CSF-1) receptor<sup>[28]</sup> and M2 to M1 macrophage re-education via small drug toll-like receptor (TLR) agonists,<sup>[29]</sup> cytokines<sup>[30]</sup> or microRNAs,<sup>[31]</sup> among others. We envision that preferential internalization of GO flakes in IBA1<sup>+</sup> cells may offer an opportunity to utilize this material as a nanocarrier that delivers the necessary cues for these and similar strategies. The great versatility that GO offers to incorporate, covalently or noncovalently, and deliver very chemically diverse payloads will likely also be an advantage toward these strategies. In addition, reports have also pointed at an intrinsic capacity of GO flakes to induce M1 to M2 macrophage polarization, although the mechanisms are still not fully understood.<sup>[32]</sup> Indeed, the interactions of GO and other graphene derived materials with the immune system are being thoroughly researched, incorporating concepts of “immunity-by-design” that aim to provide next generation immune-targeted therapeutics through rational material design.<sup>[33]</sup> Overall, strategies targeting the macrophage compartment will likely synergize with other immunotherapy, chemotherapy, and radiotherapy interventions against glioblastoma, and thus combination studies are warranted. Beyond immunotherapy, recent studies have also shown that macrophages that uptake drug-loaded nanoparticles can act as local depots for extended release of the therapeutic payload.<sup>[34]</sup>

To our knowledge, the intratumoral distribution of GO sheets throughout the human orthotopic glioblastoma xenograft mass observed in this work has not been previously reported. Other groups have pursued the intravenous administration of modified GO, functionalized either with transferrin or with iron oxide nanoparticles, in an allogeneic rat glioma model.<sup>[35]</sup> However, none of their studies has determined the translocation of GO into the brain, let alone its distribution and internalization by different cell types populating the tissue. Our studies demonstrated consistently the capacity of GO sheets to diffuse extensively throughout the entire tumor volume, both in vitro (Figures 2 and 3) and in vivo (Figure 5). In the latter, uptake by migratory macrophages and microglia may have also contributed to the distribution of the material. This extensive translocation constitutes a unique feature among different nanoparticles and adds further support to the potential of GO as a delivery vector in direct, intratumoral therapeutic strategies against glioblastoma. Indeed, even small drug molecules can suffer in terms of distal spread and transport within the brain because the ECM is very densely packed with charged proteins that can bind the molecules and inhibit their penetration into the tissue.<sup>[36]</sup> Therefore, it is of great importance to engineer delivery vectors that achieve uniform drug/gene delivery across the tumor to treat aggressive gliomas and potentially other brain disorders. We recognize that intracranial administration as utilized in this study is not the first choice in the clinic. However, stereotactic brain surgery has been used for decades and is justified in such severe and life-threatening scenario.<sup>[37]</sup> Other alternatives to consider are the administration of GO nanoparticles at the time of surgery, in the case of resectable tumors, or further functionalization of the flakes to incorporate molecules that facilitate BBB translocation.

## 4. Conclusion

We have shown here that GO flakes of controlled lateral dimensions (<1  $\mu\text{m}$ ) distribute extensively throughout the tumor mass, are scarcely uptaken into glioblastoma cells, and are preferentially internalized by macrophages and microglia. These findings suggest that GO could be utilized as a platform for the development of immunomodulation strategies against glioblastoma based on targeting the macrophage and microglia compartment. Studies that thoroughly investigate the impact of GO uptake on the macrophage phenotype and the capacity of these vectors to efficiently deliver immunomodulatory cues should follow.

## 5. Experimental Section

**Reagents and Chemicals:** Cell culture reagents and chemicals were purchased from Sigma-Aldrich (Merck, UK) unless otherwise stated.

**GO:** Biological-grade GO was produced at the University of Manchester following a modified Hummers’ method and size separation by centrifugation as previously reported.<sup>[18]</sup> GO flakes of average lateral dimensions of few hundred nm and one to three carbon atom layers in thickness were selected for this study based on their relevance to biomedical applications. Sheets of such dimensions have been termed “small GO flakes” in previous studies<sup>[18]</sup> to differentiate them from counterparts with larger or shorter lateral dimensions. Table S1 in the Supporting Information summarizes the main physicochemical properties of the specific batch of material utilized in this study, which was fully characterized in a previous study.<sup>[19]</sup> The material was confirmed endotoxin-free.

**Cell Culture:** U-87 MG human glioblastoma cell line was obtained from the American Type Culture Collection (ATCC) and authenticated at the University of Manchester. Cells were maintained in Dulbecco’s Modified Eagle’s Medium (DMEM) supplemented with 10% fetal bovine serum (FBS; Gibco, Thermo Fisher Scientific, UK) and 1% antibiotics (penicillin and streptomycin, PenStrep). For in vivo studies, U-87 MG cells were used below passage 10.

**3D Spheroid Formation:** U-87 MG cells grown as monolayers were detached into a single-cell suspension with trypsin/ethylenediaminetetraacetic acid (EDTA). 10 000 cells were seeded in each well of a 96-well plate, previously coated with 1% agar, in 200  $\mu\text{L}$  complete cell culture medium (composition above). Spheroids were left to form for 3 d before the exposure to GO flakes.

**U-87 MG Exposure to GO Flakes:** For studies with U-87 MG spheroids, cell culture medium was removed on day 3 after spheroid seeding and replaced with cell culture medium containing 10 or 100  $\mu\text{g mL}^{-1}$  of GO flakes, without FBS. U-87 MG cells grown in monolayers were also exposed to GO flakes at 10 or 100  $\mu\text{g mL}^{-1}$  concentrations without FBS. After 4 h of incubation, GO-containing medium replaced by fresh complete medium.

**Monitoring of U-87 MG Spheroid Growth:** The diameter of U-87 MG spheroids exposed to GO was measured on the day of exposure and 2, 4, 6, 8, 10, and 12 d after treatment. Images were taken with an inverted light microscope (Primovert, Zeiss), focusing on the equatorial plane. 12 spheroids were monitored per condition.

**Cell Counting from Dissociated Spheroids:** Spheroids treated with 0, 10, or 100  $\mu\text{g mL}^{-1}$  of GO flakes were dissociated into single cell suspensions 10 d after the exposure. In brief,  $n = 8$  spheroids per condition were centrifuged and treated with 0.01% trypsin/EDTA solution. Following enzymatic treatment, single cells were resuspended in complete media and cells were counted on a hemocytometer.

**Annexin V/propidium iodide (PI) Staining and Flow Cytometry:** U-87 MG cells seeded in P12-well plates (Costar, Corning) were treated with GO flakes (10 and 100  $\mu\text{g mL}^{-1}$ , 0.5 mL per well), as described above, for 24 h. After treatment, cells were detached using 0.05% trypsin–EDTA for 10 min, followed by the addition of FBS (30  $\mu\text{L}$  per well, Gibco, Thermo Fisher Scientific, UK), and collected in 1.5 mL tubes. Cells were centrifuged for 5 min at 1500 rpm and resuspended in 1X diluted Annexin-binding

buffer (200  $\mu\text{L}$  per tube, v13246, Thermo Fisher Scientific, UK). 1  $\mu\text{L}$  per tube of Annexin V (A13201, Thermo Fisher Scientific, UK) was added and incubated with the cells for 20 min in the dark. Samples were stored on ice, 1  $\mu\text{L}$  per tube of propidium iodide (P4864-10ML) was added 30 s before the analysis by FACSVerse flow cytometry using the fluorescein isothiocyanate (FITC, for Annexin V) and phycoerythrin (PE, for propidium iodide) channels. Excitation/emission wavelength: Annexin V = 495/519, propidium iodide = 493/636.

**Cryosectioning of 3D Spheroids:** Spheroids were collected and frozen in Cryomatrix embedding resin (Thermo Fisher Scientific, UK). The frozen spheroid blocks were sectioned at 10  $\mu\text{m}$  thickness using a Leica CM1510-3 cryostat (Leica Biosystems, Germany). Cryosections were placed on poly-L-lysine microscope slides (Thermo Fisher Scientific, UK) and preserved at  $-20\text{ }^{\circ}\text{C}$  until use.

**Immunohistochemical Staining (IHC):** Spheroid cryosections were fixed in pure acetone for 10 min and rehydrated in phosphate buffered saline (PBS) with 0.3% triton (PBS-T) for 15 min. Endogenous peroxidase activity was blocked by quenching with  $\text{H}_2\text{O}_2$  (3% in methanol) for 30 min. Sections were incubated with 10% normal goat serum for 30 min to prevent nonspecific binding of antibodies. Subsequently, the sections were incubated overnight with primary antibodies at  $4\text{ }^{\circ}\text{C}$ . After three washings in PBS, the biotinylated secondary antibody (Histostain-Plus IHC Kit, Invitrogen, USA) was added and incubated for 30 min at RT. Later, sections were treated with enzyme-conjugated streptavidin (Histostain-Plus IHC Kit, Invitrogen, USA) for 30 min at RT and then visualized with 3,3'-diaminobenzidine tetrahydrochloride (Invitrogen, USA). Finally, sections were counterstained with Gill's hematoxylin, dehydrated, and mounted in Entellan (Merck, Germany). Images were acquired with a microscope digital camera (DFC450, Leica, Germany) integrated into a light microscope (DM2500, Leica, Germany). Antibody information is provided in Table S9 in the Supporting Information.

**Light Sheet Fluorescence Microscopy (LSFM) of Wholemount U-87 MG Spheroids:** U-87 MG spheroids were exposed to GO in agar-coated 96 well-plates as described above and fixed for whole mount imaging 24 h after treatment. In brief, spheroids were transferred to 1.5 mL Eppendorf tubes, washed three times with PBS (10 min each), and later fixed in 4% paraformaldehyde (PFA), 0.5% triton (2.5 h at  $4\text{ }^{\circ}\text{C}$ ). After a wash in PBS for 10 min, the samples were incubated with  $6 \times 10^{-6}\text{ M}$  4',6-diamidino-2-phenylindole (DAPI) at RT for 40 min. Finally, the spheroids were washed twice in PBS (10 min each) and mounted in 1% low melting agarose in MilliQ water, in capillary tubes. For that purpose, agarose was warmed up to  $60\text{ }^{\circ}\text{C}$  and then left to cool down to  $37\text{ }^{\circ}\text{C}$  to avoid damaging the spheroids. LSFM was performed with a Lightsheet Z.1 microscope (Zeiss). DAPI was excited with the 405 nm laser line and its emission was detected using a bandpass filter (420–470 nm). GO was excited with the 561 nm laser line of the microscope and its fluorescence was recorded in 620–690 emission range. In order to remove any autofluorescence background, the microscope was manipulated to incorporate a longpass filter (Thorlabs, cutoff 850 nm).

**TEM and Toluidine Blue Staining of Ultrathin Spheroid Sections:** Spheroids were fixed in 2.5% glutaraldehyde and 4% PFA buffered with 0.1 M sodium cacodylate buffer (pH 7.4) at RT for 2 h and overnight at  $4\text{ }^{\circ}\text{C}$ . They were then washed with 0.1 M sodium cacodylate buffer and postfixed in 2% osmium tetroxide ( $\text{OsO}_4$ ). Following several washes with 0.1 M sodium cacodylate buffer, the spheroids were stained en-bloc with 2% uranyl acetate and dehydrated in a graded ethanol series. This was followed by specimen embedding in Araldite M mixtures and was performed according to standard procedures. The Araldite M blocks were then trimmed, semi-thin sectioned (150–200 nm), and stained with toluidine blue (to aid with the orientation and visualization of samples). Subsequently, thin sections were cut and transferred onto copper mesh grids. The grids were stained in 2% uranyl acetate in glass distilled water for 15 min. The grids were then secondarily stained with lead citrate for 5 min and washed with distilled water. Imaging was performed at 120 kV on a Jeol TEM, (JEM1400).

**Raman Mapping of Spheroid Sections:** Semi-thin spheroid sections prepared as described above were used for Raman spectroscopy imaging in which GO can be identified by a typical Raman spectrum characterized

by two specific D and G bands at about 1352 and 1594  $\text{cm}^{-1}$ , respectively, and a less prominent 2D band at about 2707  $\text{cm}^{-1}$ . This characteristic spectrum can be used as fingerprints to reveal the presence of GO in any matrix, including sections of spheroids embedded in resin. Herein, Raman mapping of the GO location within spheroid sections was performed using a HORIBA XploRA PLUS Raman microscope working with a 638 nm excitation wavelength. Raman mapping was performed using a 50x objective by collecting a Raman spectrum at each single pixel of the region of interest, using a 638 nm laser operating at 25% of power, through a 300  $\mu\text{m}$  hole and 100  $\mu\text{m}$  slit, and an acquisition time of 1 s for each spectrum. A step size of 2  $\mu\text{m}$  was used between each collected spectrum. Each Raman map was about 15–20 h of data collection; the size of each map was adapted to the spheroid to be mapped. Due to the increasing size of spheroids with the applied GO concentration, Raman maps of non-treated spheroids were hence made of a single map; while Raman maps of 10 and 100  $\mu\text{g mL}^{-1}$  GO treated spheroids were made of two to three and three to four maps, respectively (Figure S2, Supporting Information). Consecutive maps were slightly overlapping in order to allow stitching and reconstruction of the final map using common map features at the edges.

**Raman Image Analysis:** A convolution<sup>[38]</sup>-based fuzzy template matching algorithm was used to identify the representative peaks for GO at shifts of approximately 1352 and 1594  $\text{cm}^{-1}$  based on a template of a typical GO fingerprint. Convolution computes the “overlap” between two functions and is a standard technique in signals processing and image analysis. It is used for template matching in popular tools such as OpenCV.<sup>[39]</sup> This algorithm was implemented in Python 3.7.4 and makes extensive use of the SciPy signal library. First, data containing undefined values were excluded, and the rest were smoothed by a median filter, which removed most cosmic ray spikes. To reduce the computational load for the convolution step, spectra were filtered based on the means of shifts inside and outside the D and G bands region. Then, the individual spectra were clipped to the size of the template, such that they included the location of the characteristic GO peaks. This further reduced the computational load of the convolution step and avoided false positives due to coincidentally similar peaks at other shifts. The clipped spectra were normalized. Finally, the smoothed, filtered, clipped, and normalized spectra were convolved with the template. If the value of the maximum of the convolution was greater than a predefined threshold, then the “scipy.signal.find\_peaks” function was used to confirm the presence of the representative GO peaks. The code used is available at [https://github.com/kebarr/raman\\_analysis](https://github.com/kebarr/raman_analysis). The algorithm was validated by testing it using samples treated with different concentrations of GO, and the results are summarized in Table S3 in the Supporting Information. It can be seen that very few spectra were identified as containing GO in the case of the control (untreated) samples, and that the number of GO positive sites as a proportion of total sites in those treated with 100  $\mu\text{g mL}^{-1}$  GO was, roughly, an order of magnitude greater than in the samples treated with 10  $\mu\text{g mL}^{-1}$  GO.

**Gene Expression:** The spheroids were removed from 96-well plates and lysed by vortexing in lysis buffer from the Purelink RNA Mini Kit (Invitrogen). RNA extraction was performed following the manufacturer's instructions. cDNA was synthesized from 0.5  $\mu\text{g}$  of RNA template using the High Capacity cDNA Reverse Transcription Kit (Applied Biosystems) following the manufacturer's protocol. High throughput RT-qPCR was then performed using Fluidigm Biomark HD with a 96.96 dynamic array format. Data was normalized to the geometric mean of two reference genes (*GAPDH* and *MAPK1*) following the Livak method ( $2^{-\Delta\Delta\text{Ct}}$ ). *GAPDH* and *MAPK1* were identified as the most stable housekeeping genes implementing the Normfinder algorithm<sup>[40]</sup> (Figure S2, Supporting Information).  $n = 3$  biological replicates (each including 24 U-87 MG spheroids to obtain sufficient RNA) were analyzed in duplicates. Data are shown as fold change  $\pm$  error (Figure 1f) or in heatmaps showing the mean fold change (Figure S5, Supporting Information). Error was propagated

following the formula:  $\text{Error}(a + b) = \sqrt{\text{Error}(a)^2 + \text{Error}(b)^2}$ . Statistical analysis was performed using  $\Delta\text{Ct}$  values. A list of the genes included in the study and the primers used is provided in Table S4 in the Supporting Information.

**Mass Spectroscopy:** Spheroids (15 per group) were collected and centrifuged at 200 g for 10 min. Pellets were resuspended in lysis buffer (7 M urea, 2 M thiourea, 4% 3-((3-cholamidopropyl) dimethylammonio)-1-propanesulfonate (CHAPS), and  $20 \times 10^{-3}$  M Tris-HCl, pH 8.8) to isolate proteins. Bicinchoninic Acid (BCA) assay (Pierce, Thermo Fisher Scientific, UK) was used to quantify total protein concentration. The profiling of proteins was performed using nano Acquity ultra performance liquid chromatography coupled with LC-MS/MS system on Synapt instrument (Waters). For each sample, a total of 500 ng tryptic protein digest was used. The analysis was performed at the Acibadem Labmed Laboratories (Turkey). The data were first processed with ProteinLynx Global Server v. 2.5, IdentityE software and Progenesis v4 (Waters). Differential expression analysis and subsequent plotting was then performed in R (version 3.6.1) following the Differential Enrichment analysis of Proteomics data (DEP) package in Bioconductor: <https://bioconductor.org/packages/devel/bioc/vignettes/DEP/inst/doc/DEP.html>. From this analysis, a list of statistically significant, differentially expressed proteins is obtained. The Uniprot IDs of these proteins were converted into Entrez IDs, then Gene Ontology analysis was performed using ClusterProfiler. The list of differentially expressed proteins is included in Table S7 (upregulated) and Table S8 (downregulated) in the Supporting Information.

**Animals:** Fifteen female athymic nude-*Foxn1<sup>nu</sup>* mice were purchased from Envigo (UK), housed in individually ventilated cages in groups of 5, kept in a 12/12 h light/dark cycle with environmental enrichment and ad libitum access to food and water. All procedures were carried out in accordance with the Animal (Scientific Procedures) Act 1986 (UK), approved by the University of Manchester Ethical Review Committee and under a UK Home Office Project License 70/7763.

**U-87 MG Orthotopic Xenograft:** Fifteen female athymic nude mice (8–9 weeks old) were anaesthetized using isoflurane (3% induction and 1–2% maintenance in medical oxygen, at a rate of  $1.5 \text{ L min}^{-1}$ ) and placed in a rodent stereotactic frame. After the incision site was sterilized, a 0.7 mm bore hole was drilled above the right striatum at the following co-ordinates: 0.0 mm anterior and 2.5 mm lateral from bregma. A 10  $\mu\text{L}$  Hamilton syringe (701 RN) fitted with a 26-gauge needle was advanced to 3 mm below the cortical surface and withdrawn by 0.4 to 2.6 mm. 1  $\mu\text{L}$  PBS containing  $1 \times 10^5$  U-87 MG cells was then injected into the intracranial pocket at a rate of  $0.2 \mu\text{L min}^{-1}$ . After injection, the needle was kept in place for 3 min before being slowly extracted to limit cell build-up in the needle track.

**Intratumoral Administration of GO:** 17–21 d after tumor inoculation, mice bearing U-87 MG gliomas ( $n = 15$ ) were assigned to three experimental groups ( $n = 5$  each) for intratumoral delivery of: 5% dextrose,  $1.0 \text{ mg mL}^{-1}$  GO in 5% dextrose or  $0.1 \text{ mg mL}^{-1}$  GO in 5% dextrose, in 1  $\mu\text{L}$  total volume. Mice were anaesthetized and positioned in a stereotactic frame and a 33-gauge needle was advanced through the original bore hole to a depth of 2.6 mm below the cortical surface. The solution was delivered at a rate of  $0.2 \mu\text{L min}^{-1}$ .

**MRI Acquisition and Analysis:** MRI was performed 2, 3, and 4 weeks after tumor inoculation (5% dextrose control,  $n = 2$ ; GO  $1 \text{ mg mL}^{-1}$ ,  $n = 3$ ; GO  $0.1 \text{ mg mL}^{-1}$ ,  $n = 3$ ). MRI was conducted using a 7 Tesla magnet connected to a Bruker Advance III console (Bruker Biospin Ltd, UK). Mice were placed in a custom-built Perspex magnet capsule with a cylindrical surface coil and imaged under isoflurane anesthesia (3% induction and 1–2% maintenance in medical oxygen at a rate of  $1.5 \text{ L min}^{-1}$ ). Respiratory rate was monitored throughout imaging and anesthetic level controlled based on respiratory parameters (60–90 bpm). After localizing imaging on three orthogonal axes, the whole brain was imaged using  $T_2$  weighted MRI: Rapid Acquisition with Relaxation Enhancement (RARE) pulse sequence, repetition time = 2200 ms, echo time 33 ms, RARE factor 8, field of view (FOV)  $30 \text{ mm} \times 30 \text{ mm}$  matrix size  $512 \times 512$ , 17 contiguous slices, thickness 0.8 mm, averages = 5. Tumor volumes were determined using ImageJ software (National Institutes of Health, NIH, Bethesda, USA). Tumor area was delineated for each coronal slice and the total tumor volume generated from the acquired measurements.

**Tissue Processing and Immunohistochemistry:** Four weeks after tumor implantation, U-87 MG tumor-bearing mice ( $n = 15$ ) were anaesthetized with 4% isoflurane and culled by transcardial perfusion with heparinized PBS ( $10 \text{ units mL}^{-1}$ ), followed by 4% PFA in PBS. The brains were re-

moved and postfixed overnight at  $4^\circ\text{C}$  and later placed in sucrose solution (30% in PBS) until loss of buoyancy. The brains were snap frozen in precooled isopentane ( $-50^\circ\text{C}$ ) and coronal sections ( $20 \mu\text{m}$  thick) were taken using a cryostat (Leica CM3050, Leica Biosystems, Germany) that incorporated the entire tumor. Sections were either stained with hematoxylin and eosin (H&E) using standard protocols or immunofluorescence staining.

For the latter, frozen brain sections were fixed in 4% PFA. After fixation, blocking buffer composed of 5% normal donkey serum, 1% bovine serum albumin, and 0.2% triton in PBS was incubated with the brain sections for 1.5 h at RT. Sections were then incubated with primary antibodies at  $4^\circ\text{C}$  overnight. After washing the primary antibody (three times with PBS, 5 min each), secondary antibodies were added to the sections for 1 h. Sections were finally washed three times with PBS (5 min each) and mounted in Prolong Gold medium with DAPI. For antibody information, see Table S9 in the Supporting Information.

**Quantification of Collagen I in Brain Tumor Sections:** Collagen I was detected by immunofluorescence performed as described above. The percent of collagen I positive pixels was analyzed using Image J software (NIH, Bethesda, USA), as follows. Individual images (field of view at 20x magnification) were saved as eight-bit images. A threshold (Threshold = 6) was set on the collagen I channel in comparison with the original image. The images of collagen I staining (red pixels) and the background (black pixels) were transformed into binary images where the Collagen I staining was in black and the rest, white color. A table was generated using the “List” function in the Histogram window, showing the number of black (“0” row) and white (“255” row) pixels. The percentage of collagen I positive pixels was calculated as  $[\text{black pixels}/(\text{black} + \text{white pixels}) \times 100]$ . Three random fields of view were analyzed in each of four brain tumor tissue sections per mouse ( $n = 5$ ).

**Quantification of GO and IBA1<sup>+</sup> Cells in Brain Tumor Sections:** Immunofluorescence for IBA1<sup>+</sup> cells and human mitochondria (Mit) was performed as described above. Images were captured as z-stacks using an inverted SP8 laser scanning confocal microscope. The fields were selected using the bright field channel to detect black particles that indicate the presence of GO. Images were analyzed in Fiji (Image J software). Black particles identified as GO were drawn individually in the images obtained from GO injected brains and saved in region of interest (ROI) manager. No black particles were found in dextrose injected brains. Markings from GO particles were overlapped with the sum of the images of IBA1 staining in which black particles were in focus. The total number of GO particles and the number of GO particles that colocalized with IBA1<sup>+</sup> cells per field of view were counted and the percentage was calculated. The same quantification was used to calculate the number of GO particles in IBA1<sup>+</sup>/Mit<sup>+</sup> double positive cells.

**Statistical Analysis:** Statistical analysis was performed with GraphPad Prism (version 8) and IBM SPSS Statistics (version 25) software. A non-parametric test (Mann–Whitney) was used to analyze data that were not normally distributed. When data were normally distributed, Levene’s test was first implemented to confirm the homogeneity of variance. When the variance was homogeneous, statistically significant differences among groups were analyzed by one-way analysis of variance (ANOVA) and Tukey’s post hoc test. When the variance was not homogeneous, statistically significant differences among groups were analyzed by Welch ANOVA and Games-Howell post hoc test. The number of replicates and specific test implemented for each study are indicated in each figure legend and the relevant Experimental sections. Data are presented as mean  $\pm$  standard deviation (SD), unless otherwise specified in the figure legend.

## Supporting Information

Supporting Information is available from the Wiley Online Library or from the author.

## Acknowledgements

K.K., P.S., S.V., and M.S. would like to acknowledge the United Kingdom Research and Innovation (UKRI) Engineering and Physical Sciences

Research Council (EPSRC) for funding most of this work under the 2D-Health Programme Grant (EP/P00119X/1). K.K. and I.d.L. would also like to acknowledge the UKRI (EPSRC) for an International Centre-to-Centre grant (EP/S030719/1) between the University of Manchester and Harvard University that funded part of this work. T.K. would like to thank the UKRI (EPSRC and Medical Research Council, MRC) Center for Doctoral Training (CDT) in Regenerative Medicine (EP/L014904/1) for a funded PhD studentship. The authors would like to thank Dr. Marta Quintanilla and Dr. David Spiller for help with LSFM. The equipment at the University of Manchester Bioimaging and Genomic Technologies facilities used in this study were purchased with grants from the Biotechnology and Biological Sciences Research Council (BBSRC), Wellcome Trust, and the University of Manchester Strategic Fund. A.Y., C.G., and H.T. would like to thank the project "G-IMMUNOMICS" funded under the Joint Transnational Call (JTC) Graphene 2015. A.Y. is thankful to the Turkish Academy of Sciences (TUBA) for the financial support.

## Conflict of Interest

The authors declare no conflict of interest.

## Author Contributions

I.d.L., A.Y., and K.K. initiated, designed, and coordinated the study. I.d.L. contributed to experiments (spheroid growth, LSFM) and data analysis (gene expression, proteomics), prepared the figures and wrote the paper with contributions and feedback from coauthors. P.S. performed in vivo studies, including cell and nanomaterial administration, MRI imaging, tissue processing, staining, and imaging. C.G. and H.T. performed spheroid formation, GO treatment, and sample preparation for mass spectroscopy. A.C. and A.O. performed cryosectioning, ultrathin sectioning, immunostaining, and TEM imaging. M.S. performed immunofluorescence imaging and analysis in samples from in vivo studies. T.K. performed spheroid growth and gene expression experiments and analyzed data. Y.C. and S.V. performed GO uptake and cytotoxicity study in U87MG cells (2D monolayers). S.V. contributed to LSFM and its data analysis. K.B. performed bioinformatics analysis for Raman and proteomics data. C.B. performed the collection of Raman spectroscopy maps and initial nonalgorithm based analysis. A.Y. and K.K. had overall responsibility of the work and contributed to the writing of the paper.

## Keywords

2D materials, brain cancer, immunotherapy, macrophages, nanomedicine

Received: May 14, 2020

Revised: August 25, 2020

Published online: October 9, 2020

- [1] E. Alphantery, *Front. Pharmacol.* **2018**, *9*, 879.
- [2] N. Kaka, K. Hafazalla, H. Samawi, A. Simpkin, J. Perry, A. Sahgal, S. Das, *Cancers (Basel)* **2019**, *11*, 1723.
- [3] K. Aldape, K. M. Brindle, L. Chesler, R. Chopra, A. Gajjar, M. R. Gilbert, N. Gottardo, D. H. Gutmann, D. Hargrave, E. C. Holland, D. T. W. Jones, J. A. Joyce, P. Kearns, M. W. Kieran, I. K. Mellingshoff, M. Merchant, S. M. Pfister, S. M. Pollard, V. Ramaswamy, J. N. Rich, G. W. Robinson, D. H. Rowitch, J. H. Sampson, M. D. Taylor, P. Workman, R. J. Gilbertson, *Nat. Rev. Clin. Oncol.* **2019**, *16*, 509.
- [4] B. G. Harder, M. R. Blomquist, J. Wang, A. J. Kim, G. F. Woodworth, J. A. Winkles, J. C. Loftus, N. L. Tran, *Front. Oncol.* **2018**, *8*, 462.
- [5] a) A. Sottoriva, I. Spiteri, S. G. Piccirillo, A. Touloumis, V. P. Collins, J. C. Marioni, C. Curtis, C. Watts, S. Tavare, *Proc. Natl. Acad. Sci. U.*

- S. A. **2013**, *110*, 4009; b) A. P. Patel, I. Tirosh, J. J. Trombetta, A. K. Shalek, S. M. Gillespie, H. Wakimoto, D. P. Cahill, B. V. Nahed, W. T. Curry, R. L. Martuza, D. N. Louis, O. Rozenblatt-Rosen, M. L. Suva, A. Regev, B. E. Bernstein, *Science* **2014**, *344*, 1396.
- [6] J. D. Bernstock, J. H. Mooney, A. Ilyas, G. Chagoya, D. Estevez-Ordonez, A. Ibrahim, I. Nakano, *J. Neurosurg.* **2019**, 1. Epub ahead of print.
- [7] a) E. K. Nduom, M. Weller, A. B. Heimberger, *Neurooncology* **2015**, *17*, vii9; b) D. Hambarzumyan, D. H. Gutmann, H. Kettenmann, *Nat. Neurosci.* **2016**, *19*, 20.
- [8] a) L. B. Thomsen, T. Linemann, S. Birkelund, G. A. Tarp, T. Moos, *Materials (Basel)* **2019**, *12*; b) C. Englert, A. K. Trutzschler, M. Raasch, T. Bus, P. Borchers, A. S. Mosig, A. Traeger, U. S. Schubert, *J. Controlled Release* **2016**, *241*, 1; c) C. He, P. Cai, J. Li, T. Zhang, L. Lin, A. Z. Abbasi, J. T. Henderson, A. M. Rauth, X. Y. Wu, *J. Controlled Release* **2017**, *246*, 98.
- [9] C. Lei, Y. Cui, L. Zheng, P. K. Chow, C. H. Wang, *Biomaterials* **2013**, *34*, 7483.
- [10] A. Marino, A. Camponovo, A. Degl'Innocenti, M. Bartolucci, C. Tapeinos, C. Martinelli, D. De Pasquale, F. Santoro, V. Mollo, S. Arai, M. Suzuki, Y. Harada, A. Petretto, G. Ciofani, *Nanoscale* **2019**, *11*, 21227.
- [11] P. Saalik, P. Lingasamy, K. Toome, I. Mastandrea, L. Rousso-Noori, A. Tobi, L. Simon-Gracia, H. Hunt, P. Paiste, V. R. Kotamraju, G. Bergers, T. Asser, T. Ratsep, E. Ruoslahti, R. Bjerkvig, D. Friedmann-Morvinski, T. Teesalu, *J. Controlled Release* **2019**, *308*, 109.
- [12] T. Glaser, I. Han, L. Wu, X. Zeng, *Front. Pharmacol.* **2017**, *8*, 166.
- [13] K. Maier-Hauff, F. Ulrich, D. Nestler, H. Niehoff, P. Wust, B. Thiesen, H. Orawa, V. Budach, A. Jordan, *J. Neurooncol.* **2011**, *103*, 317.
- [14] a) D. Bitounis, H. Ali-Boucetta, B. H. Hong, D. H. Min, K. Kostarelos, *Adv. Mater.* **2013**, *25*, 2258; b) D. Yin, Y. Li, H. Lin, B. Guo, Y. Du, X. Li, H. Jia, X. Zhao, J. Tang, L. Zhang, *Nanotechnology* **2013**, *24*, 105102; c) H. Li, K. Fierens, Z. Zhang, N. Vanparijs, M. J. Schuijs, K. Van Steendam, N. Feiner Gracia, R. De Rycke, T. De Beer, A. De Beuckelaer, S. De Koker, D. Deforce, L. Albertazzi, J. Grooten, B. N. Lambrecht, B. G. De Geest, *ACS Appl. Mater. Interfaces* **2016**, *8*, 1147; d) M. Vincent, I. de Lazaro, K. Kostarelos, *Gene Ther.* **2017**, *24*, 123.
- [15] I. de Lazaro, S. Vranic, D. Marson, A. F. Rodrigues, M. Buggio, A. Esteban-Arranz, M. Mazza, P. Posocco, K. Kostarelos, *Nanoscale* **2019**, *11*, 13863.
- [16] a) H. Yue, X. Zhou, M. Cheng, D. Xing, *Nanoscale* **2018**, *10*, 1063; b) I. de Lazaro, K. Kostarelos, *Sci. Rep.* **2019**, *9*, 12520.
- [17] a) M. Wierzbicki, S. Jaworski, M. Kutwin, M. Grodzik, B. Strojny, N. Kurantowicz, K. Zdunek, R. Chodun, A. Chwalibog, E. Sawosz, *Int. J. Nanomed.* **2017**, *12*, 7241; b) M. Hinzmann, S. Jaworski, M. Kutwin, J. Jagiello, R. Kozinski, M. Wierzbicki, M. Grodzik, L. Lipinska, E. Sawosz, A. Chwalibog, *Int. J. Nanomed.* **2014**, *9*, 2409.
- [18] A. F. Rodrigues, L. Newman, N. Lozano, P. Mukherjee, B. Fadeel, C. Bussy, K. Kostarelos, *2D Mater.* **2018**, *5*.
- [19] S. P. Mukherjee, B. Lazzaretto, K. Hultenby, L. Newman, A. F. Rodrigues, N. Lozano, K. Kostarelos, P. Malmberg, B. Fadeel, *Chem* **2018**, *4*, 334.
- [20] S. Vranic, A. F. Rodrigues, M. Buggio, L. Newman, M. R. H. White, D. G. Spiller, C. Bussy, K. Kostarelos, *ACS Nano* **2018**, *12*, 1373.
- [21] a) H. Lu, M. H. Stenzel, *Small* **2018**, *14*, e1702858; b) T. Rodrigues, B. Kundu, J. Silva-Correia, S. C. Kundu, J. M. Oliveira, R. L. Reis, V. M. Correlo, *Pharmacol. Ther.* **2018**, *184*, 201.
- [22] M. Yu, Y. Yang, C. Zhu, S. Guo, Y. Gan, *Drug Discovery Today* **2016**, *21*, 1155.
- [23] M. Orecchioni, D. Bedognetti, L. Newman, C. Fuoco, F. Spada, W. Hendrickx, F. M. Marincola, F. Sgarrella, A. F. Rodrigues, C. Menard-Moyon, G. Cesareni, K. Kostarelos, A. Bianco, L. G. Delogu, *Nat. Commun.* **2017**, *8*, 1109.

- [24] a) L. C. Huysentruyt, P. Mukherjee, D. Banerjee, L. M. Shelton, T. N. Seyfried, *Int. J. Cancer* **2008**, *123*, 73; b) L. C. Huysentruyt, Z. Akgoc, T. N. Seyfried, *ASN Neuro* **2011**, *3*, 183; c) M. H. Deininger, K. Seid, S. Engel, R. Meyermann, H. J. Schluesener, *Acta Neuropathol.* **2000**, *100*, 673.
- [25] C. Bonnans, J. Chou, Z. Werb, *Nat. Rev. Mol. Cell Biol.* **2014**, *15*, 786.
- [26] a) A. Sontheimer-Phelps, B. A. Hassell, D. E. Ingber, *Nat. Rev. Cancer* **2019**, *19*, 65; b) H.-F. Tsai, A. Trubelja, A. Q. Shen, G. Bao, *J. R. Soc., Interface* **2017**, *14*, 20170137.
- [27] a) J. Kowal, M. Kornete, J. A. Joyce, *Immunotherapy* **2019**, *11*, 677; b) Y. Pires-Afonso, S. P. Niclou, A. Michelucci, *Int. J. Mol. Sci.* **2020**, *21*, 689.
- [28] M. Ovais, M. Guo, C. Chen, *Adv. Mater.* **2019**, *31*, 1808303.
- [29] C. B. Rodell, S. P. Arlauckas, M. F. Cuccarese, C. S. Garriss, R. Li, M. S. Ahmed, R. H. Kohler, M. J. Pittet, R. Weissleder, *Nat. Biomed. Eng.* **2018**, *2*, 578.
- [30] Y. Wang, Y. X. Lin, S. L. Qiao, H. W. An, Y. Ma, Z. Y. Qiao, R. P. Rajapaksha, H. Wang, *Biomaterials* **2017**, *112*, 153.
- [31] N. N. Parayath, A. Parikh, M. M. Amiji, *Nano Lett.* **2018**, *18*, 3571.
- [32] B. C. Lee, J. Y. Lee, J. Kim, J. M. Yoo, I. Kang, J. J. Kim, N. Shin, D. J. Kim, S. W. Choi, D. Kim, B. H. Hong, K. S. Kang, *Sci. Adv.* **2020**, *6*, eaaz2630.
- [33] a) A. Gazzzi, L. Fusco, M. Orecchioni, S. Ferrari, G. Franzoni, S. Yan, M. Rieckher, G. Peng, M. A. Lucherelli, I. A. Vacchi, N. D. Q. Chau, A. Criado, A. Istif, D. Mancino, A. Dominguez, H. Eckert, E. Vazquez, T. Da Ros, P. Nicolussi, V. Palermo, B. Schumacher, G. Cuniberti, Y. Mai, C. Clementi, M. Pasquali, X. Feng, K. Kostarelos, A. Yilmazer, D. Bedognetti, B. Fadeel, M. Prato, A. Bianco, L. G. Delogu, *J. Phys. Mater.* **2020**, *3*; b) M. Orecchioni, C. Menard-Moyon, L. G. Delogu, A. Bianco, *Adv. Drug Delivery Rev.* **2016**, *105*, 163; c) M. Orecchioni, V. Bordoni, C. Fuoco, G. Reina, H. Lin, M. Zoccheddu, A. Yilmazer, B. Zavan, G. Cesareni, D. Bedognetti, A. Bianco, L. G. Delogu, *Small* **2020**, *16*, e2000123.
- [34] M. A. Miller, Y. R. Zheng, S. Gadde, C. Pfirschke, H. Zope, C. Engblom, R. H. Kohler, Y. Iwamoto, K. S. Yang, B. Askevold, N. Kolishetti, M. Pittet, S. J. Lippard, O. C. Farokhzad, R. Weissleder, *Nat. Commun.* **2015**, *6*, 8692.
- [35] a) G. Liu, H. Shen, J. Mao, L. Zhang, Z. Jiang, T. Sun, Q. Lan, Z. Zhang, *ACS Appl. Mater. Interfaces* **2013**, *5*, 6909; b) S. Shirvalilou, S. Khoei, S. Khoei, S. R. Mahdavi, N. J. Raoufi, M. Motevalian, M. Y. Karimi, *J. Photochem. Photobiol., B* **2020**, *205*, 111827.
- [36] D. J. Wolak, R. G. Thorne, *Mol. Pharmaceutics* **2013**, *10*, 1492.
- [37] P. J. Kelly, *Neurosurgery* **2000**, *46*, 16.
- [38] S. W. Smith, *The Scientist and Engineer's Guide to Digital Signal Processing*, California Technical Publishing, San Diego, CA **1997**.
- [39] G. Bradski, *Dr Dobb's J. Software Tools* **2000**, *25*, 120.
- [40] C. L. Andersen, J. L. Jensen, T. F. Orntoft, *Cancer Res.* **2004**, *64*, 5245.